
Paper:

Sevilla, R., Fernández-Méndez, S. & Huerta, A. (in press). 3D NURBS-enhanced finite element method (NEFEM). *International Journal for Numerical Methods in Engineering, 88*(2), 103-125.
http://dx.doi.org/10.1002/nme.3164

3D NURBS-Enhanced Finite Element Method (NEFEM)

Ruben Sevilla, Sonia Fernández-Méndez, Antonio Huerta

Laboratori de Càlcul Numèric (www-lacan.upc.edu), Departament de Matemàtica Aplicada III, E.T.S. de Ingenieros de Caminos, Canales y Puertos, Universitat Politècnica de Catalunya, Jordi Girona 1, E-08034 Barcelona, Spain.

Abstract

This paper presents the extension of the recently proposed NURBS-Enhanced Finite Element Method (NEFEM) to 3D domains. NEFEM is able to exactly represent the geometry of the computational domain by means of its CAD boundary representation with Non-Uniform Rational B-Splines (NURBS) surfaces. Specific strategies for interpolation and numerical integration are presented for those elements affected by the NURBS boundary representation. For elements not intersecting the boundary, a standard finite element rationale is used, preserving the efficiency of classical FEM. In 3D NEFEM special attention must be paid to geometric issues that are easily treated in the 2D implementation. Several numerical examples show the performance and benefits of NEFEM compared to standard isoparametric or cartesian finite elements. NEFEM is a powerful strategy to efficiently treat curved boundaries and it avoids excessive mesh refinement to capture small geometric features.

Keywords: NURBS, accurate geometry representation, CAD, Finite Elements, Discontinuous Galerkin, high-order isoparametric approximations

---

1. INTRODUCTION

Research in finite element methods (FEMs) with an accurate or exact geometric representation of the computational domain has received increasing

---

Email addresses: `ruben.sevilla@upc.edu` (Ruben Sevilla), `sonia.fernandez@upc.edu` (Sonia Fernández-Méndez), `antonio.huerta@upc.edu` (Antonio Huerta)

Preprint of
R. Sevilla, S. Fernández-Méndez and A. Huerta
3D NURBS-Enhanced Finite Element Method
International Journal for Numerical Methods in Engineering, 88 (2); 103-125, 2011

attention in the last years, see among others [1, 2, 3]. The standard FE technique in domains with curved boundaries is the isoparametric FEM, in which curved boundaries are approximated using piecewise polynomial parametrizations, see [4]. Geometric approximation induced by isoparametric FEs may lead to an important loss of accuracy, specially when high-order approximations are considered, see [5]. In this situation, mesh refinement to accurately capture geometry may compromise the benefits of using high-order approximations.

Non-uniform rational B-splines (NURBS, see [6]) are nowadays widely used for geometric description in Computer Aided Design (CAD). Other popular options for geometric description in CAD are polynomial B-splines (a particular case of NURBS) and subdivision surfaces. This fact has motivated the development of novel numerical techniques considering CAD descriptions of the computatoinal domain.

Isogeometric methods have become very popular in the last decade, see [1, 7, 8, 9, 10, 11] to name a few. These methods consider a CAD description of the entire computational domain and the solution is approximated using the same basis used for the CAD representation of the geometry.

NURBS-Enhanced Finite Element Method uses NURBS to accurately describe the boundary of the computational domain, but it differs from isogeometric methods in two main facts. First, NURBS are used to describe the boundary of the computational computational domain, not the entire domain as done in isogeometric methods. Secondly, the solution is approximated using polynomials and the approximation is defined with cartesian coordinates, directly in the physical space. From a practical point of view, NEFEM considers efficient strategies for numerical integration on elements affected by curved boundaries. The basis of NEFEM in 2D are presented in [12], showing the advantages in front of classical isoparametric FEs using both continuous and discontinuous Galerkin formulations. See also [13] for the application of NEFEM to the numerical solution of inviscid flow problems. Several high-order FE methodologies for the treatment of curved boundaries are discussed and compared in [5], including isoparametric FEM, cartesian FEM, p-FEM and NEFEM. Numerical examples show that NEFEM is not only more accurate than FE methods with an approximate boundary representation, but also outperforms p-FEM with an exact boundary representation, showing the advantages of combining cartesian approximation with exact boundary representation.

This paper focuses on the extension of NEFEM to 3D domains. Although conceptually easy, the extension of NEFEM to 3D requires attention to several geometric aspects. It is important to remark that all the ideas presented here are valid not only when the boundary of the domain is parametrized by NURBS, but for any piecewise boundary parametrization. The discussion is centered on NURBS boundary parametrization because they are the most extended technology in CAD. Section 2 introduces basic concepts on NURBS surfaces. The extension of NEFEM to 3D domains is presented in Section 3. Curved elements and faces are defined in terms of the NURBS boundary representation of the domain. This section also presents the strategy to approximate the solution and to perform the numerical integration in those elements affected by NURBS boundaries. The strategy presented here allows a straightforward treatment of trimmed and singular NURBS surfaces. Section 4 presents and discusses several numerical examples, which are solved using a piecewise continuous (standard FE) or discontinuous formulations. These examples show not only the performance and benefits of the proposed method for simple geometries, but also the possibilities of NEFEM when very small geometric features induce drastic mesh refinement with standard finite elements.

2. BASIC CONCEPTS ON NURBS SURFACES

NURBS surfaces are piecewise rational functions defined in parametric form. NURBS allow representing a wide range of surfaces, and contrary to polynomial B-Splines or subdivision surfaces, they allow to represent conics exactly. Basic concepts on NURBS surfaces are recalled in this section, see [6] for a complete presentation.

A NURBS surface of degree q in λ and degree l in κ, is a piecewise rational parametrization

$$\boldsymbol{S}(\lambda,\kappa) = \left(\sum_{i=0}^{\mathtt{n}^{\lambda}_{\mathtt{cp}}} \sum_{j=0}^{\mathtt{n}^{\kappa}_{\mathtt{cp}}} \nu_{ij}\, \boldsymbol{B}_{ij}\, S^{q,l}_{i,j}(\lambda,\kappa) \right) \Bigg/ \left(\sum_{i=0}^{\mathtt{n}^{\lambda}_{\mathtt{cp}}} \sum_{j=0}^{\mathtt{n}^{\kappa}_{\mathtt{cp}}} \nu_{ij}\, S^{q,l}_{i,j}(\lambda,\kappa) \right) \qquad 0 \leq \lambda,\kappa \leq 1,$$

where $\{\boldsymbol{B}_{ij}\}$ are the coordinates of the $(\mathtt{n}^{\lambda}_{\mathtt{cp}}+1)(\mathtt{n}^{\kappa}_{\mathtt{cp}}+1)$ *control points* (defining the *control net*), $\{\nu_{ij}\}$ are the control weights, and $\{S^{q,l}_{i,j}(\lambda,\kappa)\}$ are the 2D B-spline basis functions of degree q in λ and l in κ. Each 2D B-Spline basis function is defined as a tensor product of 1D basis functions, that is

$$S^{q,l}_{i,j}(\lambda,\kappa) := C^{\Lambda^{\lambda}}_{i,q}(\lambda)\, C^{\Lambda^{\kappa}}_{j,l}(\kappa), \tag{1}$$

Preprint of
R. Sevilla, S. Fernández-Méndez and A. Huerta
3D NURBS-Enhanced Finite Element Method
International Journal for Numerical Methods in Engineering, 88 (2); 103-125, 2011

where, for instance in the λ direction, 1D B-spline basis functions are recursively defined as

$$C_{i,0}^{\Lambda^\lambda}(\lambda) = \begin{cases} 1 & \text{if } \lambda \in [\lambda_i, \lambda_{i+1}[, \\ 0 & \text{elsewhere,} \end{cases}$$
$$C_{i,k}^{\Lambda^\lambda}(\lambda) = \frac{\lambda - \lambda_i}{\lambda_{i+k} - \lambda_i} C_{i,k-1}^{\Lambda^\lambda}(\lambda) + \frac{\lambda_{i+k+1} - \lambda}{\lambda_{i+k+1} - \lambda_{i+1}} C_{i+1,k-1}^{\Lambda^\lambda}(\lambda),$$

for $k = 1 \dots q$, where λ_i, for $i = 0, \dots, \mathtt{n}_{\mathtt{k}}^{\lambda}$, are the *knots* or *breakpoints*, assumed ordered $0 \leq \lambda_i \leq \lambda_{i+1} \leq 1$. They form the so-called *knot vector*

$$\Lambda^\lambda = \{\underbrace{0, \dots, 0}_{q+1}, \lambda_{q+1}, \dots, \lambda_{\mathtt{n}_{\mathtt{k}}^{\lambda} - q - 1}, \underbrace{1, \dots, 1}_{q+1}\},$$

which uniquely describes B-spline basis functions. The multiplicity of a knot, when it is larger than one, determines the decrease in the number of continuous derivatives. The number of control points, $\mathtt{n}_{\mathtt{cp}}^{\lambda}+1$, and knots, $\mathtt{n}_{\mathtt{k}}^{\lambda}+1$, are related to the degree of the parametrization, q, by the relation $\mathtt{n}_{\mathtt{k}}^{\lambda} = \mathtt{n}_{\mathtt{cp}}^{\lambda}+q+1$, see [6] for more details. Figure 1 shows two 2D B-spline basis functions for knot vectors

$$\Lambda^\lambda = \{0, 0, 0, 0, 0.4, 1, 1, 1, 1\},$$
$$\Lambda^\kappa = \{0, 0, 0, 0.2, 0.6, 0.6, 1, 1, 1\}.$$

Complete 1D basis are represented for each direction to illustrate the construction of 2D basis functions (1).

Note that NURBS surfaces change their definition along *knot lines*, that is when $\lambda = \lambda_i$, for $i = 1, \dots, \mathtt{n}_{\mathtt{k}}^{\lambda}$, or $\kappa = \kappa_i$, for $i = 1, \dots, \mathtt{n}_{\mathtt{k}}^{\kappa}$. An example of a NURBS surface is represented in Figure 2, with the corresponding control net. Knot lines are represented on the NURBS surface in order to stress the piecewise nature of the parametrization.

Trimmed NURBS surfaces, defined as the original parametrization restricted to a subspace of the parametric space, are common in practical applications. An example of a trimmed NURBS surface is represented in Figure 3, showing the NURBS surface of Figure 2 trimmed with the thick curve. In practical applications, it is also common to deal with *singular* (or *singularly parametrized*) NURBS surfaces. Such surfaces contain at least one *singular point*, defined as a point where a directional derivative is zero. For these surfaces, knot lines typically converge to the singular point, see an example in Figure 4.

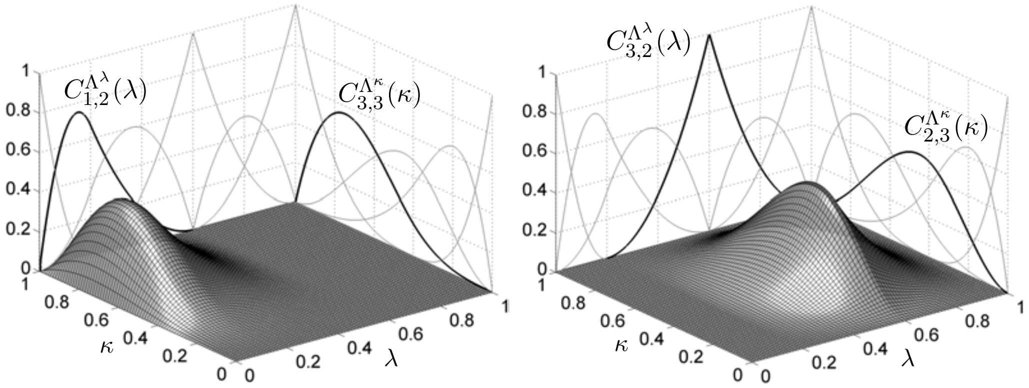

(a) $S^{2,3}_{1,3}(\lambda,\kappa) := C^{\Lambda^\lambda}_{1,2}(\lambda)C^{\Lambda^\kappa}_{3,3}(\kappa)$ (b) $S^{2,3}_{3,2}(\lambda,\kappa) := C^{\Lambda^\lambda}_{3,2}(\lambda)C^{\Lambda^\kappa}_{2,3}(\kappa)$

Figure 1: Example of 2D B-spline basis functions

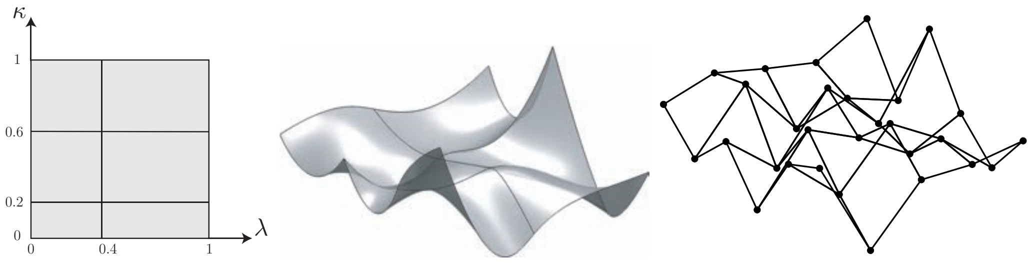

(a) (b) (c)

Figure 2: (a) Parametric space, (b) NURBS surface with knot lines, and (c) control net

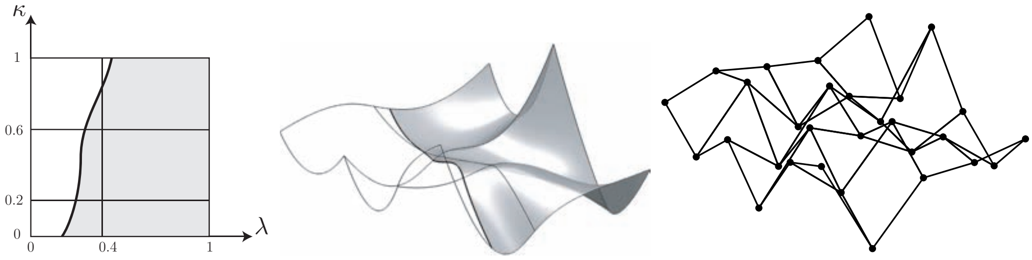

(a) (b) (c)

Figure 3: (a) Parametric space trimmed by the thick curve, (b) trimmed NURBS surface with knot lines and the thick curve used to trim the initial surface of Figure 2, and (c) control net

(a) (b) (c)

Figure 4: (a) Parametric space, (b) singular NURBS surface with knot lines, and (c) control net

3. 3D NEFEM

Consider an open bounded domain $\Omega \subset \mathbb{R}^3$ whose boundary $\partial\Omega$, or a portion of it, is defined by NURBS surfaces. Every NURBS surface is assumed to be parametrized by

$$\boldsymbol{S} : [0,1]^2 \longrightarrow \boldsymbol{S}([0,1]^2) \subseteq \partial\Omega \subset \mathbb{R}^3.$$

A regular partition of the domain $\overline{\Omega} = \bigcup_e \overline{\Omega}_e$ in tetrahedrons is assumed, such that $\Omega_i \bigcap \Omega_j = \emptyset$, for $i \neq j$. For instance, Figure 5 shows a computational domain with part of the boundary defined by NURBS surfaces corresponding to the NASA almond [14], a useful geometry for benchmarking electromagnetic scattering codes. A cut through an unstructured tetrahedral mesh is also represented in Figure 5, including the surface triangular mesh on the almond.

As usual in FE mesh generation codes, it is assumed that every curved boundary face belongs to a unique NURBS. That is, one element face can not be defined by portions of two, or more, different NURBS surfaces. Note however that the piecewise definition of each NURBS is independent on the mesh discretization. Thus, NURBS parametrization can change its definition within one face, that is, FE edges do not need to coincide with knot lines. Figure 6 shows the image of the knot lines of the NASA almond surfaces and the surface triangulation corresponding to the mesh represented in Figure 5. It can be observed that spatial discretization is independent of the piecewise NURBS surface parametrization. It is worth remarking that allowing knot lines to be independent on the spatial discretization means that special at-

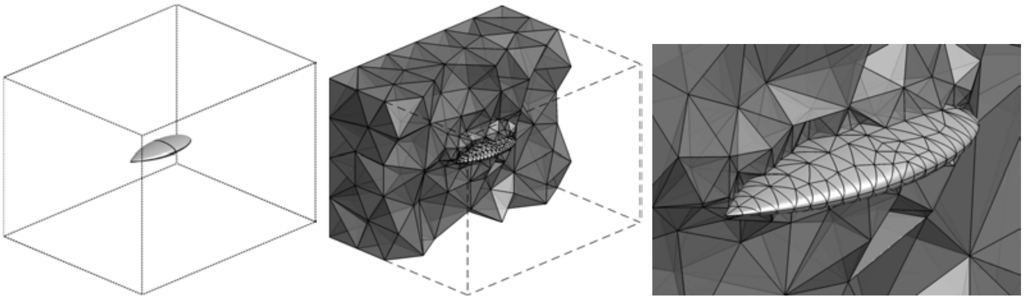

(a) (b) (c)

Figure 5: (a) Domain with part of the boundary defined by curved NURBS surfaces corresponding to the NASA almond, (b) cut through an unstructured tetrahedral mesh with the surface triangular mesh on the almond, and (c) detail of the mesh near the almond

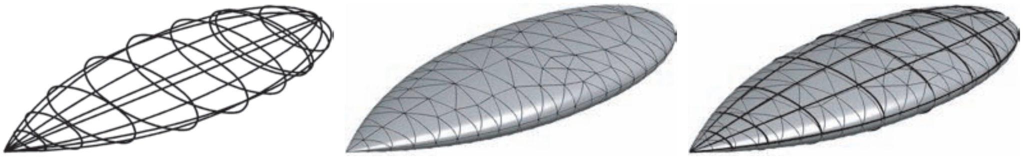

(a) (b) (c)

Figure 6: (a) Knot lines of the NURBS surfaces defining the NASA almond, (b) surface triangulation, and (c) surface triangulation and knot lines

tention must to be paid to the numerical integration over elements affected by the NURBS boundary representation, see Section 3.3.

An element without any edge or face in contact with NURBS boundaries has planar faces and it is defined and treated as a standard FE. Therefore, in the vast majority of the domain, interpolation and numerical integration are standard, preserving the computational efficiency of classical FEM. Specifical numerical strategies for interpolation and numerical integration are needed only for those elements affected by NURBS boundaries.

3.1. Curved elements

In NEFEM, curved elements are defined in terms of the NURBS boundary representation of the domain. The formal definition of curved faces and elements in a NEFEM tetrahedral mesh is given in this section.

Let Υ_e be a tetrahedral face on the NURBS boundary parametrized by $\boldsymbol{S}$, and $\boldsymbol{x}_1, \boldsymbol{x}_2, \boldsymbol{x}_3 \in \partial\Omega$ the three vertices on the NURBS boundary, see Figure 7. Assuming that the vertices $\boldsymbol{x}_1, \boldsymbol{x}_2, \boldsymbol{x}_3$ do not correspond to singular points of the NURBS parametrization, a straight-sided triangle Λ_e in the parametric space of the NURBS is uniquely defined by the parametric coordinates of the vertices, $\boldsymbol{S}^{-1}(\boldsymbol{x}_1)$, $\boldsymbol{S}^{-1}(\boldsymbol{x}_2)$ and $\boldsymbol{S}^{-1}(\boldsymbol{x}_3)$. The curved face with a NURBS boundary representation, Υ_e, is defined as the image of the straight-sided triangle Λ_e by the NURBS parametrization $\boldsymbol{S}$,

$$\Upsilon_e := \boldsymbol{S}(\Lambda_e), \tag{2}$$

as illustrated in Figure 7.

Note that when the surface $\boldsymbol{S}$ is trimmed by a curve $\boldsymbol{C}$ in the parametric space of the NURBS, the edges of the triangle Λ_e must be replaced by trimmed NURBS curves. In such cases Λ_e is a curved triangle in the parametric space of the NURBS and curved edges of Λ_e are NURBS curves (used to trim the original surface), see an example in Figure 8. Finally, assuming that one of the vertices of the tetrahedral face corresponds to a singular point of the NURBS parametrization, Λ_e must be defined as a quadrilateral in the parametric space of the NURBS, see an example in Figure 9.

Interior curved faces with an edge on the NURBS boundary are defined as a convex linear combination of the curved edge and the interior face node. For instance, curved face Υ_e^E represented in Figure 7 is parametrized by

$$\begin{aligned} \boldsymbol{\Theta}_{\boldsymbol{x_4}} \; : [\varrho_1, \varrho_2] \times [0,1] &\longrightarrow \Upsilon_e^E \\ (\varrho, \sigma) &\longmapsto \boldsymbol{\Theta}_{\boldsymbol{x_4}}(\varrho, \sigma) := (1-\sigma)\boldsymbol{\theta}(\varrho) + \sigma \boldsymbol{x}_4, \end{aligned} \tag{3}$$

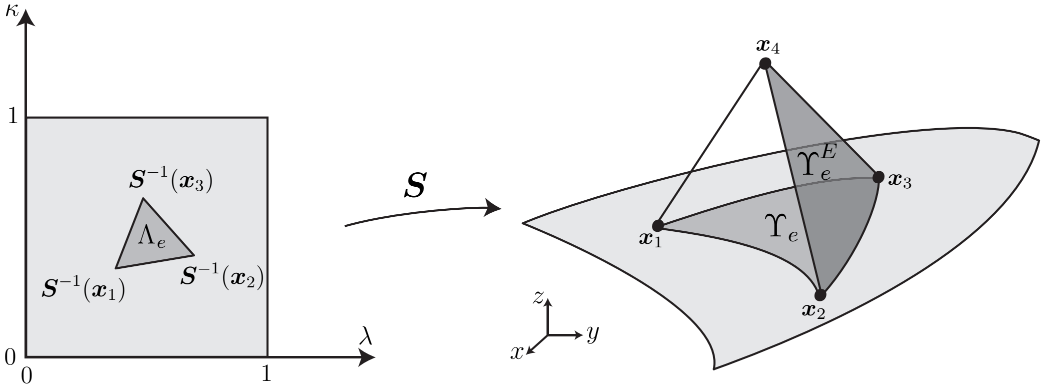

Figure 7: Curved tetrahedral element with a face on the NURBS boundary, showing a face Υ_e on the NURBS boundary, and a face Υ_e^E with an edge on the NURBS boundary, Υ_e^E

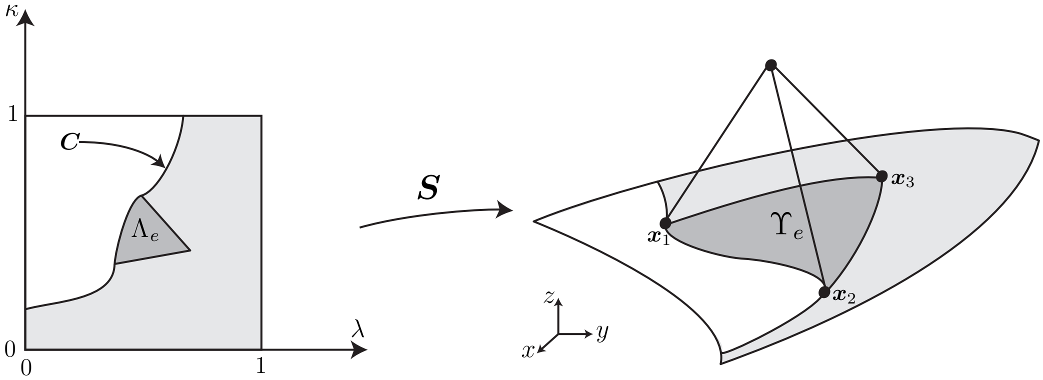

Figure 8: Curved tetrahedral face on a trimmed NURBS boundary. NURBS surface S is trimmed by NURBS curve C, leading to a curved triangle Λ_e in the parametric space

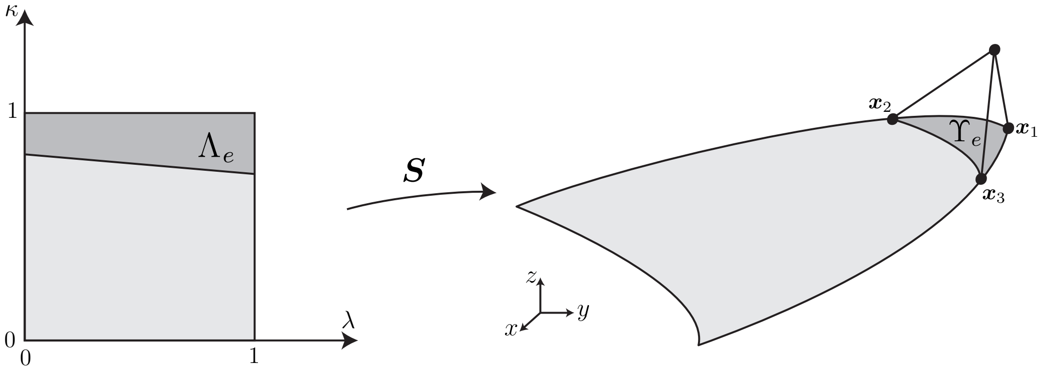

Figure 9: Curved tetrahedral face on a singular NURBS boundary with a singular point, leading to a quadrilateral Λ_e in the parametric space

where $\boldsymbol{\theta}([\varrho_1, \varrho_2])$ parametrizes the curved edge from vertex $\boldsymbol{x}_2$ to vertex $\boldsymbol{x}_3$. Note that this approach to define interior curved faces ensures the same definition of an interior curved face as seen from the two elements sharing this face. Note also that other types of curved faces are present in real meshes, such as faces with several edges over the NURBS boundary. The definition of all possible curved faces is presented in Section 3.3.

With this definition of curved faces, a curved tetrahedral element with a face on the NURBS boundary corresponds to a convex linear combination of the curved NURBS face and the interior vertex. For instance, element represented in Figure 7 is parametrized by

$$\begin{aligned} \boldsymbol{\Psi} \ &: \Lambda_e \times [0,1] \longrightarrow \Omega_e \\ &(\lambda, \kappa, \vartheta) \longmapsto \boldsymbol{\Psi}(\lambda, \kappa, \vartheta) := (1-\vartheta)\boldsymbol{S}(\lambda, \kappa) + \vartheta \boldsymbol{x}_4, \end{aligned} \tag{4}$$

where $\boldsymbol{x}_4$ denotes the interior vertex of Ω_e. Similarly, an element with an edge on the NURBS boundary corresponds to a convex linear combination of one of its curved faces and the opposite node, and can be parametrized by

$$\begin{aligned} \boldsymbol{\Phi} \ &: [\varrho_1, \varrho_2] \times [0,1]^2 \longrightarrow \Omega_e \\ &(\varrho, \sigma, \tau) \longmapsto \boldsymbol{\Phi}(\varrho, \sigma, \tau) := (1-\tau)\boldsymbol{\Theta}_{\boldsymbol{x_3}}(\varrho, \sigma) + \tau \boldsymbol{x}_4, \end{aligned} \tag{5}$$

where $\boldsymbol{x}_3$ and $\boldsymbol{x}_4$ are the interior vertices of Ω_e, see Figure 10. Note that the definition of $\boldsymbol{\Phi}$ in (5) is independent on the order of the interior vertices $\boldsymbol{x}_3$ and $\boldsymbol{x}_4$. That is, element Ω_e can be equivalently parametrized by

$$\boldsymbol{\Phi}(\varrho, \sigma, \tau) := (1-\tau)\boldsymbol{\Theta}_{\boldsymbol{x_4}}(\varrho, \sigma) + \tau \boldsymbol{x}_3.$$

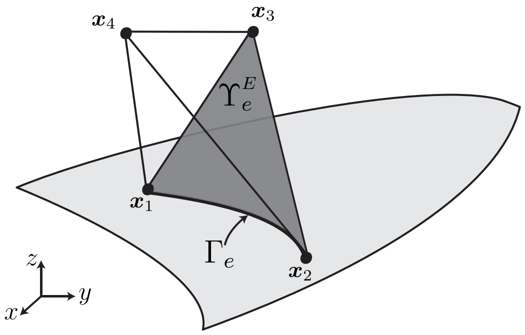

Figure 10: Curved tetrahedral element with an edge on the NURBS boundary

It is worth remarking that interior edges,(i.e, edges with no more than one node over the NURBS boundary) are considered as straight edges. Note that this assumption allows to ensure that the elements affected by the NURBS boundary representation of the domain are only elements with at least one face or one edge over the NURBS boundary, and therefore, the overhead introduced by NEFEM is restricted to a very small portion of the total number of elements.

3.2. Polynomial interpolation

NEFEM considers nodal polynomial interpolation in each element. To ensure reproducibility of polynomials in the physical space, NEFEM defines the approximation directly with cartesian coordinates, $\boldsymbol{x} = (x, y, z)^T$, that is

$$u(\boldsymbol{x}) \simeq u^h(\boldsymbol{x}) = \sum_{i=1}^{\mathtt{n_{en}}} u_i N_i(\boldsymbol{x}), \tag{6}$$

where u_i are nodal values, N_i are polynomial shape functions (Lagrange polynomials) of order p in $\boldsymbol{x}$, and $\mathtt{n_{en}}$ is the number of element nodes. Recall that in isoparametric FEM or p-FEM the approximation is defined in a reference element. However, contrary to NEFEM, the definition of the polynomial basis for high-order curved elements does not ensure reproducibility of polynomials in the physical space.

Different options can be considered to define a nodal distribution in Ω_e. Any nodal distribution, such as equally-spaced nodal distributions, can be defined on the tetrahedral with planar faces given by the vertices of Ω_e, or adapted to the NURBS geometry, see Figure 11. The definition of a nodal

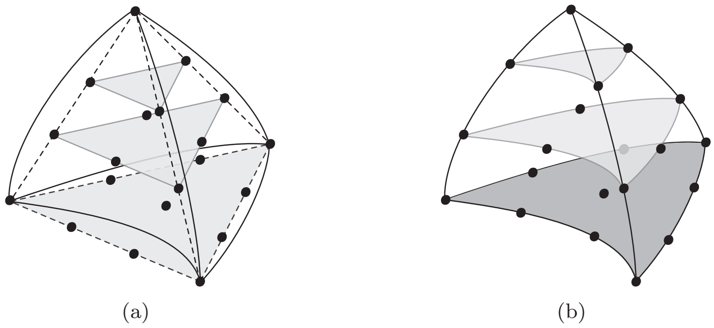

Figure 11: Equally-spaced nodal distribution for $p = 3$ (a) defined using the tetrahedral with planar faces represented by discontinuous lines, and (b) adapted to the curved geometry

distribution on the tetrahedral with planar faces, see Figure 11 (a), induces a marginal extra efficiency [12], avoiding a specific nodal distribution for each curved element. Adapting a nodal distribution to the NURBS geometry, see Figure 11 (b), allows a seamless imposition of boundary conditions in strong form, directly imposing the value of the solution at nodes on the boundary. But, nodal distributions adapted to curved boundaries do not represent any implementation advantage if boundary conditions are imposed in weak form, as usual in DG formulations. Note however the evolution of the condition number, shown in Figure 12, for the element mass matrix as a function of the polynomial degree of approximation, p. Adapted distributions of nodes induce an important reduction on condition number. In the example of Figure 11, the use of nodal distributions non-adapted to the NURBS boundary implies that some nodes lie outside the region of interest (i.e., the volume that defines the curved element). Shape functions associated to those nodes contribute very little to the elemental mass matrix deteriorating its condition number. The problem is far more evident as the degree of the approximation is increased because more nodes lie outside the region of interest.

For very high-order approximations, let say $p > 5$, equally-spaced nodal distributions may lead to ill-conditioned elemental matrices, even if adapted distributions are considered. In this case, specific nodal distributions should be implemented in Ω_e, see for instance the distributions proposed in [15, 16, 17] for elements with planar faces. Adaptation of such distributions to the curved geometry may lead to an extra reduction in condition number of the elemental matrices, see for instance [12]. An example of such distributions in

R. Sevilla, S. Fernández-Méndez and A. Huerta
3D NURBS-Enhanced Finite Element Method
International Journal for Numerical Methods in Engineering, 88 (2); 103-125, 2011

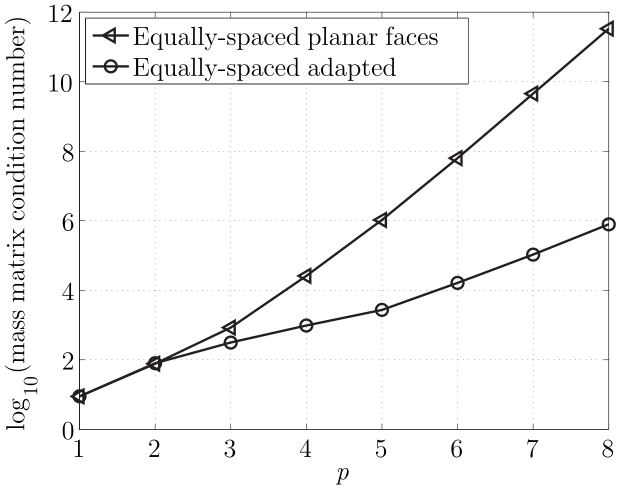

Figure 12: Condition number of the mass matrix as a function of the interpolation degree (p)

the tetrahedral element with planar faces and adapted to the curved geometry is represented in Figure 13, corresponding to distribution proposed in [16] for $p = 3$.

It is worth remarking that nodal distributions are used to define the polynomial approximation in the physical space (i.e., with Cartesian coordinates). Even if the nodes are placed over an imaginary tetrahedral with planar faces, the approximation is only defined on the interior of the element with the NURBS boundary representation.

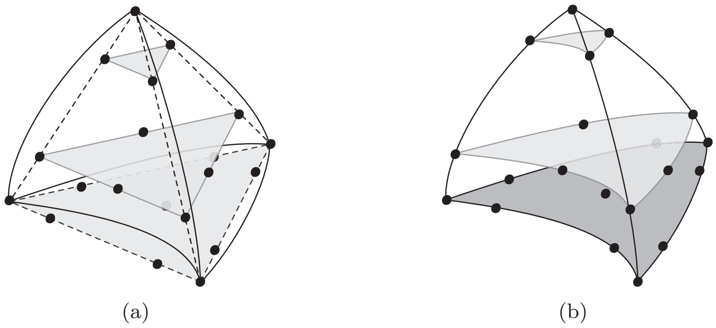
(a)
(b)

Figure 13: Nodal distribution proposed by [16] for $p = 3$ (a) defined in the tetrahedral with planar faces represented by discontinuous lines, and (b) adapted to the curved geometry

Preprint of
R. Sevilla, S. Fernández-Méndez and A. Huerta
3D NURBS-Enhanced Finite Element Method
International Journal for Numerical Methods in Engineering, 88 (2); 103-125, 2011

3.3. *Numerical integration*

Weak form of the problem requires both integrations over element faces and in element interiors. Integrals in elements not having an edge or face in contact with NURBS boundaries are computed using standard procedures. For an element Ω_e affected by the NURBS boundary representation, design of specific quadratures is necessary. Special attention must be paid to the definition of suitable quadratures accounting for changes of NURBS parametrization within an element face or edge.

Next sections present numerical integration on curved faces (surface integrals, usually related to the implementation of natural boundary conditions or to flux evaluation over the face in a DG context) and in curved elements (volume integrals).

3.3.1. *Surface integrals*

Curved faces on a NEFEM tetrahedral mesh can be classified in boundary faces or curved faces with at least one edge on a NURBS boundary. To reduce casuistics in the implementation (i.e., to avoid implementing a different parametrization for each curved face), faces with several edges on different NURBS boundaries are split in *subfaces* with only one edge on a NURBS boundary. It is worth remarking that subdivisions are only applied to design a numerical quadrature without a special treatment of each face typology, no new degrees of freedom are introduced.

To illustrate the proposed strategy, let us consider a face with two edges on different NURBS boundaries, see Figure 14. Curved face Υ_e^E is split in three *subfaces*, which are defined as a linear convex combination of the edges of Υ_e^E and its center of mass $\boldsymbol{x}_C^F$, see Figure 14. After subdivision each *subface* has at most one edge on a NURBS boundary. In the example of Figure 14, two subfaces have one edge on a NURBS boundary, and the third face, given by $\boldsymbol{x}_2$, $\boldsymbol{x}_1$ and $\boldsymbol{x}_C^F$, is planar.

With this splitting technique, it is only necessary to describe the strategy to perform the numerical integration on curved boundary faces and curved faces with only one edge on a NURBS boundary.

A surface integral on a curved boundary face $\Upsilon_e = \boldsymbol{S}(\Lambda_e)$, see Figure 7, can be written as

$$\int_{\Upsilon_e} f \, dA = \int_{\Lambda_e} f\big(\boldsymbol{S}(\lambda,\kappa)\big)\, \|J_{\boldsymbol{S}}(\lambda,\kappa)\| \, dA, \tag{7}$$

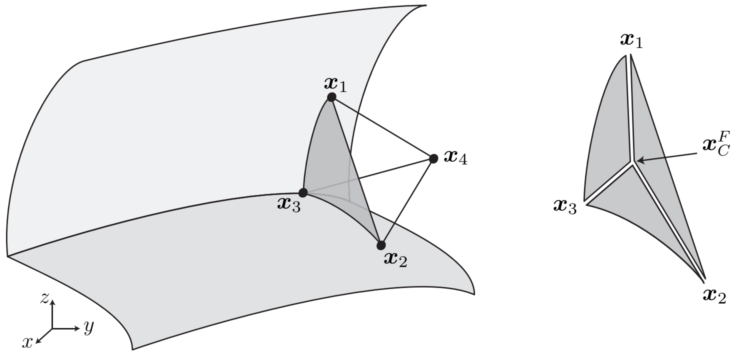

Figure 14: Tetrahedral element with two edges on different NURBS boundaries, and face splitting used for numerical integration (no new degrees of freedom are introduced)

where f is a generic function (here a polynomial) and $\|J_{\boldsymbol{S}}(\lambda,\kappa)\|$ denotes the norm of the differential of the NURBS parametrization $\boldsymbol{S}$ (which, in general, is not a polynomial). An efficient option to evaluate integral (7) is to use a triangle quadrature [18] in Λ_e. Recall that the spatial discretization is independent on the NURBS boundary representation. Therefore, a boundary face can be intersected by knot lines of the NURBS surface, see Figure 6. If changes of NURBS parametrization are present within the parametric triangle Λ_e, numerical quadrature must be designed to account for the piecewise NURBS parametrization. For instance, a triangulation of Λ_e such that each *subtriangle* has no changes of NURBS parametrization can be considered, with the associated composite quadrature (triangle quadrature in each *subtriangle*), see Figure 15.

An integral on a curved face Υ_e^E with an edge on the NURBS boundary, see Figure 7, can be written as

$$\int_{\Upsilon_e^E} f \, dA = \int_{\varrho_1}^{\varrho_2} \int_0^1 f\big(\boldsymbol{\Theta}(\varrho,\sigma)\big) \, \|J_{\boldsymbol{\Theta}}(\varrho,\sigma)\| \, dA, \tag{8}$$

where f is a generic function and $\|J_{\boldsymbol{\Theta}}(\varrho,\sigma)\|$ denotes the norm of the differential of mapping $\boldsymbol{\Theta}$, see Equation (3), which in general is not a polynomial. Numerical integration can be performed using 1D Gauss-Legendre quadratures in each direction. In fact, application $\boldsymbol{\Theta}$ is linear in the second parameter, σ, and exact integration is feasible in this direction. For a NEFEM solution with a degree of approximation p, integral (8) can be exactly computed for this direction, using a Gauss-Legendre quadrature with

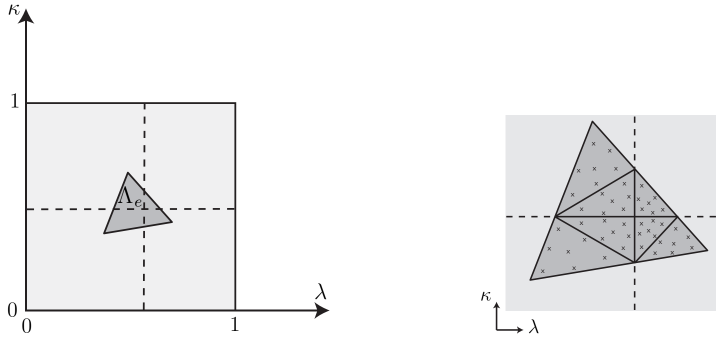

(a)

(b)

Figure 15: Definition of a numerical quadrature on Λ_e for the numerical integration on a curved tetrahedral face with changes of NURBS parametrization along discontinuous lines (knot lines): (a) triangle in the parametric space and (b) detailed view of the composite quadrature

$p+1$ integration points. Numerical integration for the first direction, given by NURBS parameter ϱ, presents the same difficulty as integration over a NURBS curve.

As usual, the evaluation of integral (8) requires taking into account the piecewise nature of the NURBS parametrization, considering composite quadratures for ϱ direction.

3.3.2. Volume integrals

Curved elements on a NEFEM tetrahedral mesh can be classified in elements with at least one face or one edge a NURBS boundary. To reduce casuistics in the implementation, elements with several faces and/or edges on different NURBS boundaries are split in *subelements* with only one face or one edge on a NURBS boundary. Again, it is worth remarking that subdivisions are only applied to design a numerical quadrature without a special treatment of each element typology, no new degrees of freedom are introduced.

Two examples are presented to illustrate the proposed strategy. First example considers a tetrahedral element with two edges on different NURBS boundaries, see Figure 14. To design a numerical quadrature on Ω_e, three *subelements* are defined as a linear convex combination of the *subfaces* and interior vertex of the element, $\boldsymbol{x}_4$, see Figure 16. In this example, two *subelements* have one edge on a NURBS boundary and the third one has planar

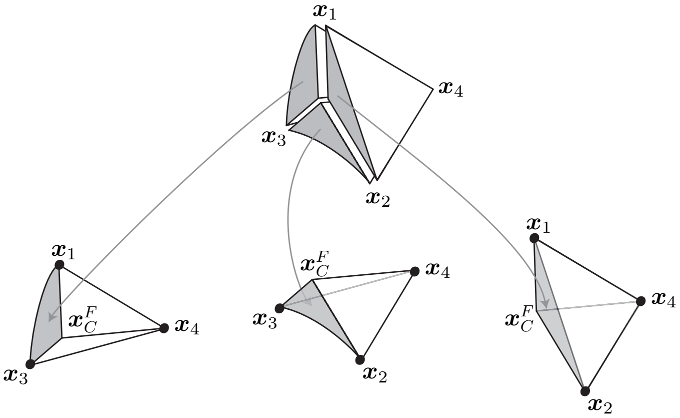

Figure 16: Splitting used for numerical integration in an element with two edges defined by different NURBS (no new degrees of freedom are introduced)

faces. Second example considers an element Ω_e with two faces on different NURBS boundaries, as represented in Figure 17. To perform numerical integration in Ω_e, the element is split in four *subelements* using its center of mass, $\boldsymbol{x}_C^E$. *Subelements* are defined as a linear convex combination of $\boldsymbol{x}_C^E$ and original faces of Ω_e, having at most one face on a NURBS boundary.

By combination of these two subdivision strategies, any element with several faces and/or edges on the NURBS boundary can be split into elements with only one face or one edge on the NURBS boundary. Thus, it is only necessary to describe the strategy to perform the numerical integration on these two element typologies.

Volume integrals for an element with one face on a NURBS boundary are performed using parametrization (4) as

$$\int_{\Omega_e} f \, dV = \int_{\Lambda_e} \int_0^1 f\big(\boldsymbol{\Psi}(\lambda, \kappa, \vartheta)\big) \, |J_{\boldsymbol{\Psi}}(\lambda, \kappa, \vartheta)| \, dV,$$

where f is a generic function (here a polynomial), and $|J_{\boldsymbol{\Psi}}|$ denotes the determinant of the Jacobian of transformation $\boldsymbol{\Psi}$. A numerical quadrature on $\Lambda_e \times [0,1]$ is easily defined as a tensor product of a triangle quadrature in Λ_e and a 1D Gauss-Legendre quadrature in $[0,1]$, see Figure 18. In fact, exact integration is feasible in third parameter due to the linearity of $\boldsymbol{\Psi}$ with respect to ϑ. For a NEFEM solution with a degree of approximation p, exact integration in this direction is provided by a Gauss-Legendre quadrature with $p+2$ integration points. To account for changes of NURBS parametrization,

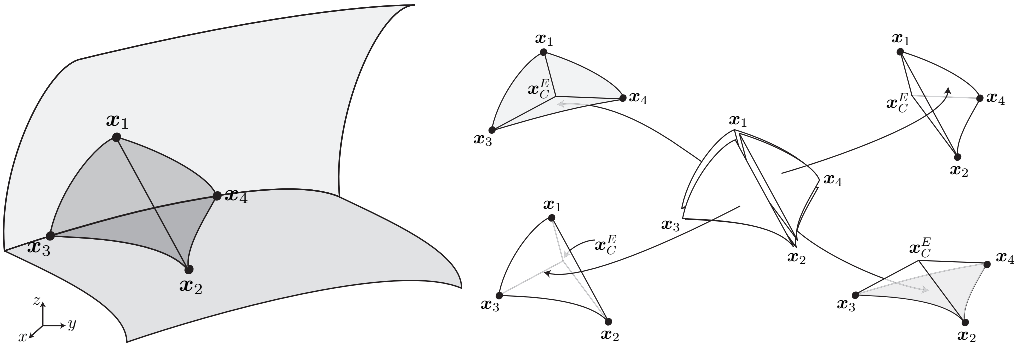

Figure 17: Splitting used for numerical integration in an element with two faces defined by different NURBS (no new degrees of freedom are introduced)

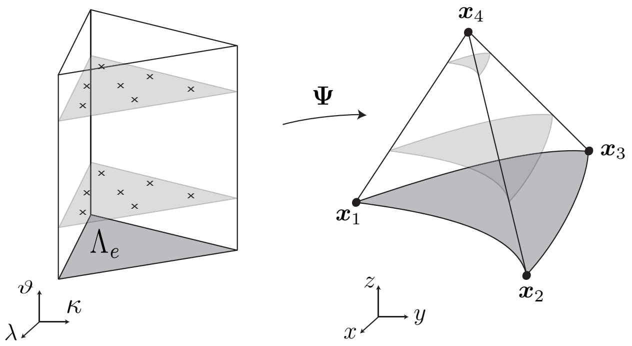

Figure 18: Transformation from $\Lambda_e \times [0, 1]$ to Ω_e to perform numerical integration on an element with a face on the NURBS boundary

Preprint of
R. Sevilla, S. Fernández-Méndez and A. Huerta
3D NURBS-Enhanced Finite Element Method
International Journal for Numerical Methods in Engineering, 88 (2); 103-125, 2011

only the quadrature in Λ_e must be modified as described in Section 3.3.1, see Figure 15. This represents an important advantage compared to numerical integration for p-FEM with NURBS, see [5] for further details.

Similarly, for an element with one edge on a NURBS boundary, volume integrals are performed using parametrization (5) as

$$\int_{\Omega_e} f \; dV = \int_{\varrho_1}^{\varrho_2} \int_0^1 \int_0^1 f\big(\boldsymbol{\Phi}(\varrho,\sigma,\tau)\big) \; |J_{\boldsymbol{\Phi}}(\varrho,\sigma,\tau)| \; dV,$$

where $|J_{\boldsymbol{\Phi}}|$ is the determinant of the Jacobian of transformation $\boldsymbol{\Phi}$. Note that application $\boldsymbol{\Phi}$ is linear in second and third parameters, σ and τ. Therefore, integrals involved in the elemental matrices, for a NEFEM solution with interpolation of degree p, can be exactly computed for these directions using a Gauss-Legendre quadrature with $p+2$ integration points. No exact integration is feasible in NURBS parameter ϱ, and composite quadratures must be considered if changes of NURBS parametrization are present.

4. NUMERICAL EXAMPLES

Application of NEFEM is illustrated using several 3D examples. First a second-order elliptic problem is solved using a standard continuous Galerkin formulation. More complex applications, involving the numerical solution of transient Maxwell's equations are also presented, and they are solved in a DG framework.

4.1. Second-order elliptic problem

The behavior of NEFEM in a continuous Galerkin framework is illustrated using the following second-order elliptic problem:

$$\left\{ \begin{array}{rcll} -\Delta u + u & = & s & \text{in} \quad \Omega \\ \nabla u \cdot \boldsymbol{n} & = & g_n & \text{on} \quad \partial\Omega, \end{array} \right. \tag{9}$$

where Ω is a sphere of unit radius and $\boldsymbol{n}$ is the outward unit normal vector to $\partial\Omega$. The analytical solution is $u(x,y) = x\cos(y) + y\sin(z) + z\cos(x)$, and the source term s is determined by analytical differentiation of u. Neumann boundary conditions corresponding to the analytical normal flux are imposed in $\partial\Omega$. A coarse mesh with only eight curved tetrahedral elements is considered, see Figure 19, and high-order approximations are introduced to properly capture the solution.

Preprint of
R. Sevilla, S. Fernández-Méndez and A. Huerta
3D NURBS-Enhanced Finite Element Method
International Journal for Numerical Methods in Engineering, 88 (2); 103-125, 2011

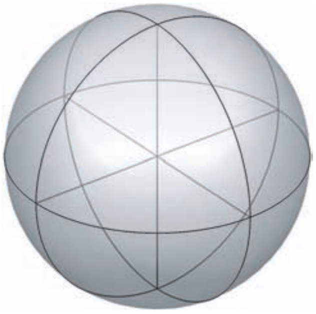

Figure 19: Coarse mesh of the sphere with eight curved tetrahedrons

Figure 20 shows cartesian FEM and NEFEM solutions with quadratic and cubic approximation. The piecewise polynomial approximation of the curved boundary introduced by isoparametric mapping is clearly observed. With quadratic FEs, the maximum difference between exact and approximated boundaries is 0.1037. For cubic approximation, geometric error is still important, 0.0268. Moreover, the piecewise polynomial approximation of the boundary induces a loss of regularity. Recall that the exact boundary $\partial\Omega$ is a $\mathcal{C}^\infty$ surface, whereas its piecewise isoparametric approximation $\partial\Omega^h$ is only $\mathcal{C}^0$ across boundary edges, see Figures 20 (a) and (c). NEFEM exactly describes the sphere boundary with one quadratic singular NURBS, independently of the spatial discretization (i.e. the polynomial degree of approximation), as represented in Figures 20 (b) and (d).

Figure 21 shows a p-convergence comparison when the polynomial order of approximation is uniformly increased starting with $p = 2$ and for the discretization shown in Figure 19. Errors in maximum and energy norms are represented as a function of the cube root of the number of degrees of freedom ($\mathtt{n_{dof}}$). For NEFEM, the expected (exponential) convergence for a problem with a smooth solution is obtained, whereas a much slower convergence is obtained for methods with an approximate boundary representation. Note that cartesian and isoparametric FEs offer the same performance if error is measured in maximum norm. However, when error is measured in energy norm, cartesian FEs perform slightly better. The definition of the polynomial basis in cartesian coordinates offers a better approximation of derivatives compared to isoparametric FEs, see [5] for more details. Figure 21 (a) also depicts maximum geometric error (measured as the maximum distance between true boundary $\partial\Omega$ and its approximation $\partial\Omega^h$), revealing

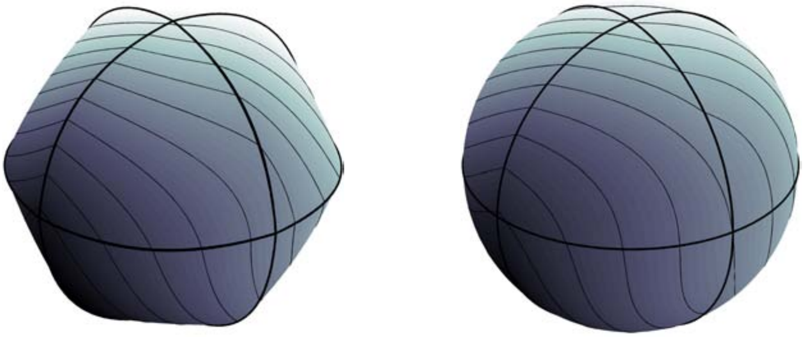

(a) FEM p=2 (b) NEFEM p=2

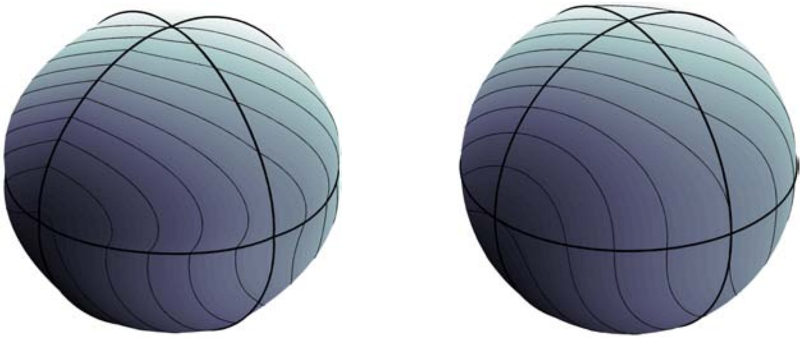

(c) FEM p=3 (d) NEFEM p=3

Figure 20: Second-order elliptic problem: surface plot of cartesian FEM and NEFEM solutions using quadratic and cubic approximations

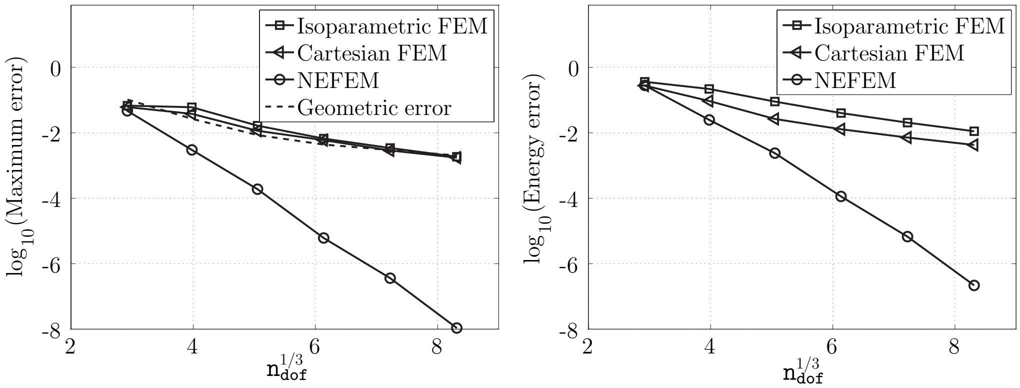

(a) (b)

Figure 21: p-convergence comparison for the second-order elliptic problem. The polynomial degree of the approximation is uniformly increased from $p = 2$ and the error is measured (a) in the maximum norm and (b) in the energy norm

that geometric error controls solution error if an approximated boundary representation is considered (isoparametric FEM or cartesian FEM).

This example stress the importance of geometrical model in FE simulations and critical conclusions are derived. In [19], p-FEM with an exact boundary description is compared to high-order subparametric elements (with a quadratic approximation of the boundary). Two dimensional examples confirm the expected exponential convergence of p-FEM, whereas subparametric approach leads to a suboptimal convergence rate. The 3D example shown in this section shows a more dramatic situation because NEFEM is compared to high-order isoparametric and cartesian elements. Therefore, this example demonstrate that a high-order approximation of the geometry is not always sufficient to achieve maximum performance for a given spatial discretization.

Remark 1. *As usual, for any formulation using Cartesian approximation, the reader should be aware that the continuity of the solution across internal curved faces is not guaranteed by imposing the continuity of the solution at face nodes. Optimal nodal distributions on curved internal faces can be used in order to guarantee optimal convergence or extra constraints must be imposed in order to guarantee the continuity of the solution across internal faces. This difficulty does not appear if a DG framework because the continuity of the solution is weakly imposed, with numerical fluxes.*

Preprint of
R. Sevilla, S. Fernández-Méndez and A. Huerta
3D NURBS-Enhanced Finite Element Method
International Journal for Numerical Methods in Engineering, 88 (2); 103-125, 2011

4.2. Electromagnetic scattering

In this section a DG formulation is considered for the simulation of 3D scattering of a single plane wave by a *perfect electric conductor* (PEC) obstacle, assumed to be surrounded by free space. For a linear isotropic material of relative permittivity ε and relative permeability μ, 3D Maxwell's equations can be written as a system of conservation laws

$$\frac{\partial \boldsymbol{U}}{\partial t} + \frac{\partial \boldsymbol{F}_k(\boldsymbol{U})}{\partial x_k} = \boldsymbol{0}, \tag{10}$$

where Einstein notation is assumed. Vector of conserved variables $\boldsymbol{U}$ and fluxes $\boldsymbol{F}_k$ are defined as

$$\boldsymbol{U} = \begin{pmatrix} \varepsilon \boldsymbol{E} \\ \mu \boldsymbol{H} \end{pmatrix}, \quad \boldsymbol{F}_1 = \begin{pmatrix} 0 \\ H_3 \\ -H_2 \\ 0 \\ -E_3 \\ E_2 \end{pmatrix}, \quad \boldsymbol{F}_2 = \begin{pmatrix} -H_3 \\ 0 \\ H_1 \\ E_3 \\ 0 \\ -E_1 \end{pmatrix}, \quad \boldsymbol{F}_3 = \begin{pmatrix} H_2 \\ -H_1 \\ 0 \\ -E_2 \\ E_1 \\ 0 \end{pmatrix},$$

where $\boldsymbol{E} = (E_1, E_2, E_3)^T$ and $\boldsymbol{H} = (H_1, H_2, H_3)^T$ are *scattered* electric and magnetic field intensity vectors.

Remark 2. *In the conservative form of Maxwell's equations* (10) *divergence-free conditions have been neglected, see [20, 21]. It is well known that, although in the continuous case divergence-free conditions are derived from* (10) *(provided the initial condition is divergence-free), this is not true in the discrete case. Nevertheless, spurious fields caused by the negligence of divergence-free conditions are easily avoided using an incident field correction described in [22].*

In the DG implementation, an element-by-element discontinuous approximation is considered and communication between elements is performed by using numerical fluxes, see [23]. At interior faces numerical fluxes are defined from Rankine-Hugoniot jump conditions, which can be interpreted as a flux splitting technique, see [24]. At exterior faces numerical flux definition depends on boundary conditions. For instance, at a PEC boundary, the tangential component of total electric field (scattered plus incident) vanish, that is

$$\boldsymbol{n} \times (\boldsymbol{E} + \boldsymbol{E}^I) = 0.$$

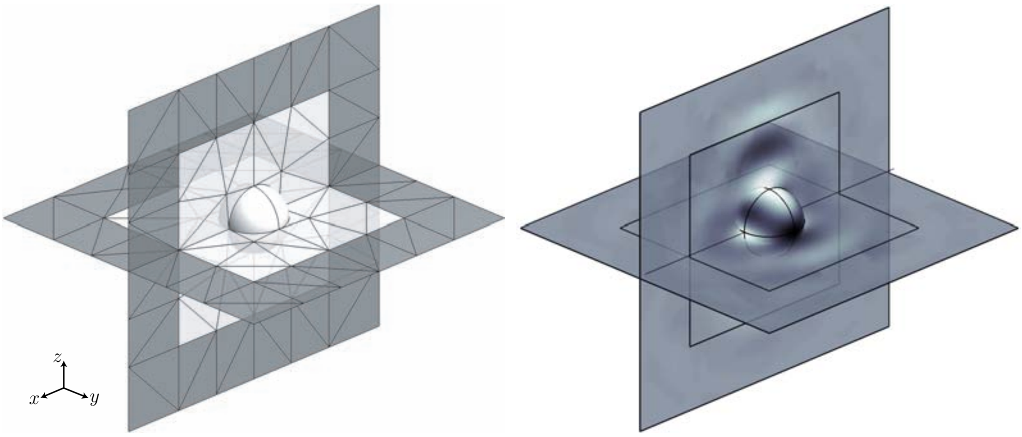

(a) (b)

Figure 22: Scattering by a PEC sphere of diameter λ: (a) two cuts of a coarse mesh with a 2λ thick PML, and (b) E_1 field for a NEFEM solution with $p = 5$

At the artificially truncated boundary a *Perfectly Matched Layer* (PML) [25] is employed to absorb outgoing waves and a characteristic boundary condition is used to terminate the PML region, see [26].

The *radar cross section* (RCS) is one of the most important quantities of interest in electromagnetic scattering problems. It provides a description of how an object reflects an incident electromagnetic wave and it is defined by RCS$= 10\log_{10}(\chi)$, where χ is the *scattering width*, see [20, 21, 25] for more details. The RCS is used in numerical examples to evaluate NEFEM performance.

4.2.1. PEC sphere

First example considers an incident plane wave traveling in z^+ direction and scattered by a PEC sphere of diameter equal to the wave length λ. The analytical solution for this problem can be found in [20, 21].

With NEFEM, the sphere is exactly described with a quadratic singular NURBS surface, and a coarse mesh with only eight elements for the discretization of the curved boundary is considered, see two cuts of the volume mesh and the surface mesh on the sphere in Figure 22 (a). The mesh has 1 271 elements with planar faces and 32 curved elements. Scattered E_1 field computed with NEFEM and a polynomial approximation of degree $p = 5$ is represented in Figure 22 (b), showing the field intensity on the sphere surface

R. Sevilla, S. Fernández-Méndez and A. Huerta
3D NURBS-Enhanced Finite Element Method
International Journal for Numerical Methods in Engineering, 88 (2); 103-125, 2011

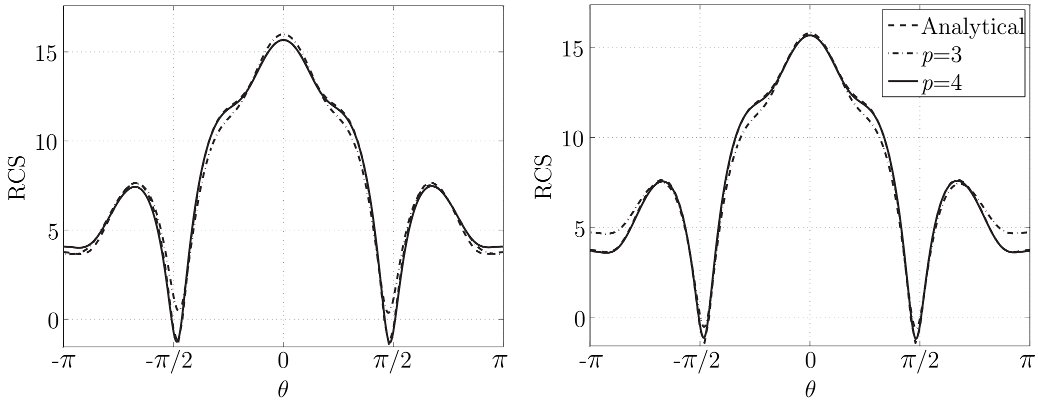

(a) Cartesian FEM (b) NEFEM

Figure 23: Scattering by a PEC sphere of diameter λ: bistatic RCS comparison for increasing p and for the vertical polarization

and illustrating the absorption of outgoing waves in the PML.

Figures 23 and 24 compare bistatic RCS computed with cartesian FEs and NEFEM for a degree of approximation $p = 3$ and $p = 4$ to the analytical solution, for vertical and horizontal polarizations respectively. For cartesian FEs, RCS error is not reduced for all viewing angles as p increases. In particular, RCS near viewing angles $-\pi$ and π is more accurate with $p = 3$ than using $p = 4$, see Figures 23 (a) and 24 (a). This discrepancy is caused by differences in the piecewise polynomial approximation of the boundary with $p = 3$ and $p = 4$. For the coarse mesh considered here, approximate boundary representation has a critical influence in scattered field distribution, and therefore in RCS patterns. With NEFEM, RCS error is decreased for all viewing angles as the degree of approximation is increased from $p = 3$ to $p = 4$ due to the exact boundary representation. In particular, a perfect match between analytical and computed solution is observed for $p = 4$, see Figures 23 (b) and 24 (b).

Note that cartesian FEs offer a slightly different performance for vertical and horizontal polarizations. In fact, higher errors are observed for horizontal polarization, whereas for NEFEM almost identical performance is observed for both polarizations. To compare accuracy, Figure 25 represents RCS error in $\mathcal{L}^2(-\pi,\pi)$ norm for increasing p, starting with $p = 2$, showing the superiority of NEFEM compared to cartesian FEs. Most critical difference is observed in horizontal polarization for $p = 5$, NEFEM is almost one order

Preprint of
R. Sevilla, S. Fernández-Méndez and A. Huerta
3D NURBS-Enhanced Finite Element Method
International Journal for Numerical Methods in Engineering, 88 (2); 103-125, 2011

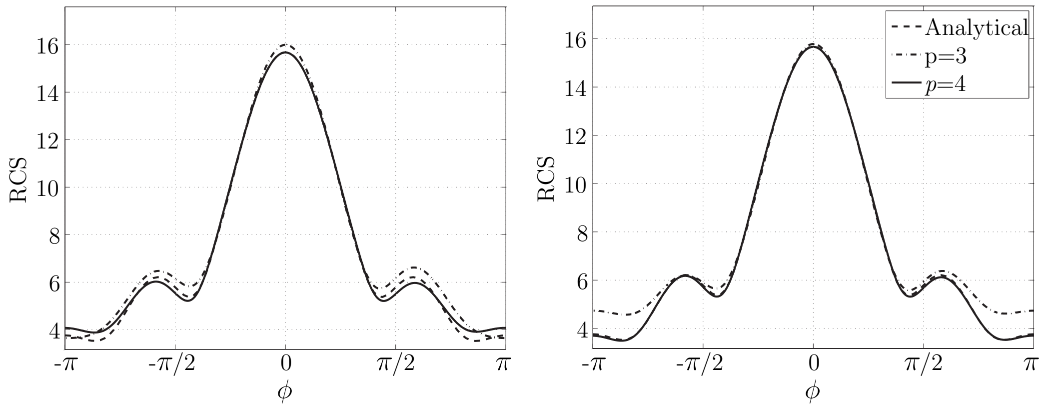

(a) Cartesian FEM (b) NEFEM

Figure 24: Scattering by a PEC sphere of diameter λ: bistatic RCS comparison for increasing p and for the horizontal polarization

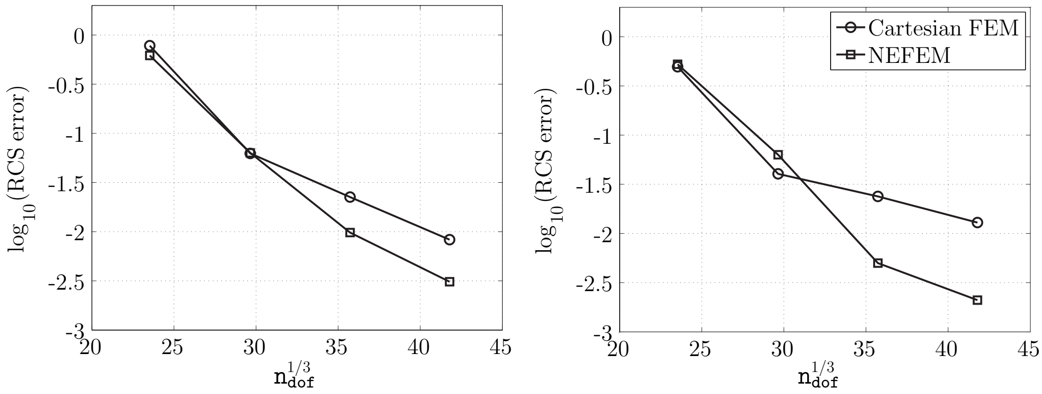

(a) Vertical polarization (b) Horizontal polarization

Figure 25: Scattering by a PEC sphere of diameter λ: p-convergence comparison of the RCS error

Preprint of
R. Sevilla, S. Fernández-Méndez and A. Huerta
3D NURBS-Enhanced Finite Element Method
International Journal for Numerical Methods in Engineering, 88 (2); 103-125, 2011

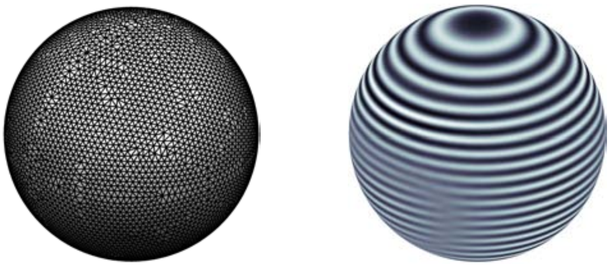

(a) Surface mesh (b) E_1

Figure 26: Scattering by a PEC sphere of diameter 20λ

of magnitude more precise than corresponding cartesian FEs.

Compared to other techniques, NEFEM is also more accurate and efficient. For instance, to achieve an accuracy of 10^{-2} measuring scattering width error in maximum norm, high-order edge elements require more than 100 000 degrees of freedom [27]. With NEFEM, a degree of approximation $p = 4$ provides an error of 4.7×10^{-3}, using 45 605 degrees of freedom. That is, NEFEM is two times more accurate by using 50% of the $\mathtt{n_{dof}}$, showing that NEFEM is also competitive compared to other techniques used by computational electromagnetics (CEM) community.

Next example considers the scattering of an incident wave traveling in the z^+ direction by a PEC sphere of diameter 20λ. The mesh used has 124 135 elements with planar faces and 17 856 curved elements. The surface mesh on the sphere is represented in Figure 26 (a), and the first component of scattered electric field over the sphere for a NEFEM solution with $p = 5$ is represented in Figure 26 (b). A comparison between computed and analytical bistatic RCS is depicted in Figure 27, showing an excellent agreement. In fact, RCS distributions overlap for viewing angles in $[-\pi/4, \pi/4]$, see Figure 28. Note also that very small differences are observed for other viewing angles. The RCS error in the $\mathcal{L}^2(-\pi, \pi)$ norm is 2.2×10^{-2} for the vertical polarization and 2.5×10^{-2} for the horizontal polarization.

It is worth recalling that even if the surface mesh of the obstacle is refined for high frequency simulations, an accurate geometric description is still important. With standard FEs the approximated surface of the obstacle is only $\mathcal{C}^0$ at boundary edges. These geometric singularities may cause important discrepancies in computed scattered field and this effect becomes more important as frequency increases, see [28].

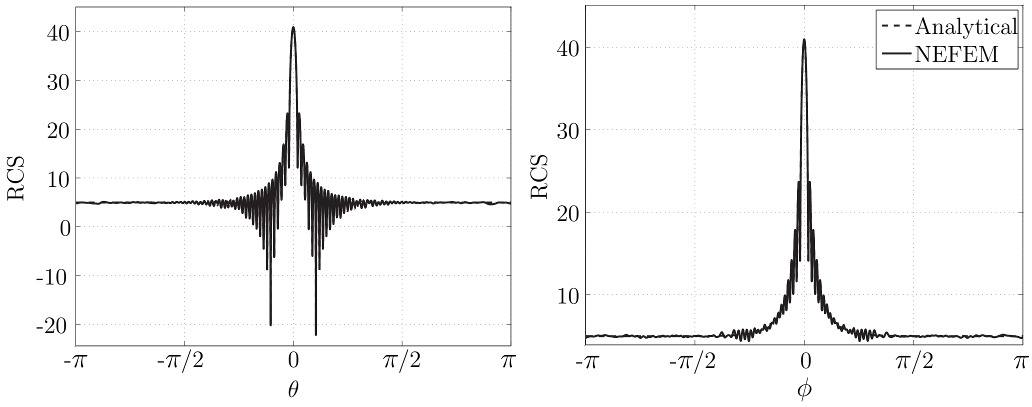

(a) Vertical polarization (b) Horizontal polarization

Figure 27: Scattering by a PEC sphere of diameter 20λ: bistatic RCS for a NEFEM solution with $p = 4$

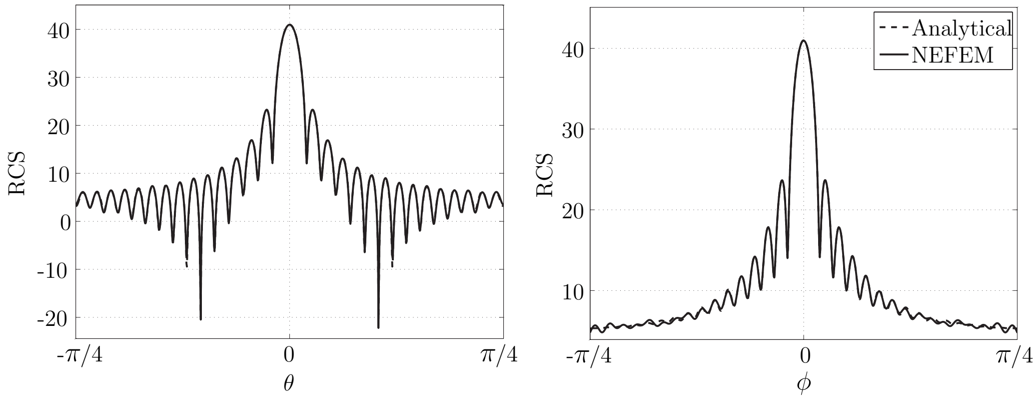

(a) Vertical polarization (b) Horizontal polarization

Figure 28: Scattering by a PEC sphere of diameter 20λ: bistatic RCS in the range $[-\pi/4, \pi/4]$ for a NEFEM solution with $p = 4$

Preprint of
R. Sevilla, S. Fernández-Méndez and A. Huerta
3D NURBS-Enhanced Finite Element Method
International Journal for Numerical Methods in Engineering, 88 (2); 103-125, 2011

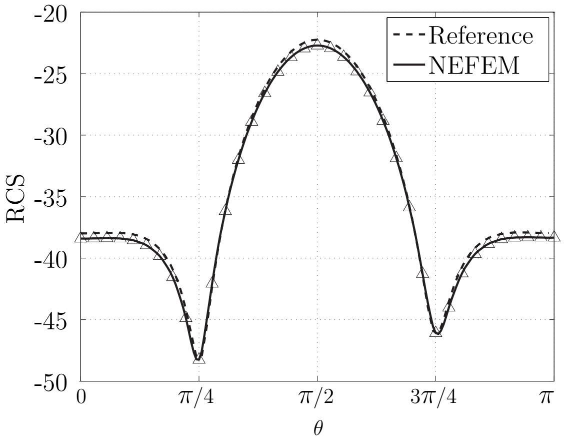

Figure 29: Scattering by a PEC NASA almond of characteristic length λ: monostatic RCS for a NEFEM solution with $p = 4$, compared with high-order edge elements [30]

4.2.2. PEC NASA almond

Following example considers a popular benchmark for 3D RCS computations, the scattering by a PEC NASA almond, see [14, 29]. One of the challenges of this example is the solution singularity on the tip of the almond. Moreover, the high variations on surface curvature introduce extra difficulty to obtain accurate RCS patterns.

First, monostatic RCS computation of an almond of characteristic length λ is considered. The mesh has 10 805 elements with planar faces and 336 curved elements. The evaluation of monostatic RCS is performed by computing $N = 36$ solutions corresponding to a series of incident angles $\theta^j = j\pi/N$, with $j = 0, \ldots, N$. Monostatic RCS for vertical polarization is represented in Figure 29, and compared with a reference solution, showing excellent agreement. Difference between both RCS patterns is 1.5×10^{-2} in the $\mathcal{L}^2(-\pi, \pi)$ norm. Reference data corresponds to published results in [30], which are obtained using high-order edge elements with non-uniform degree of approximation on a tetrahedral mesh with 4 723 elements. In NEFEM computation, markers correspond to 36 computations, and continuous line corresponds to standard postprocess of the monostatic data described in [31].

Next example considers the scattering of a plane electromagnetic wave by a PEC NASA almond of characteristic length 8λ. The mesh has 9 348 elements with planar faces and 1 200 curved elements. The surface mesh on the almond is represented in Figure 30 (a), and a detailed view of two

(a) Surface mesh (b) E_3 (c) H_3

Figure 30: Scattering by a PEC NASA almond of characteristic length 8λ: surface mesh and two components of the scattered field for a NEFEM solution with $p = 5$

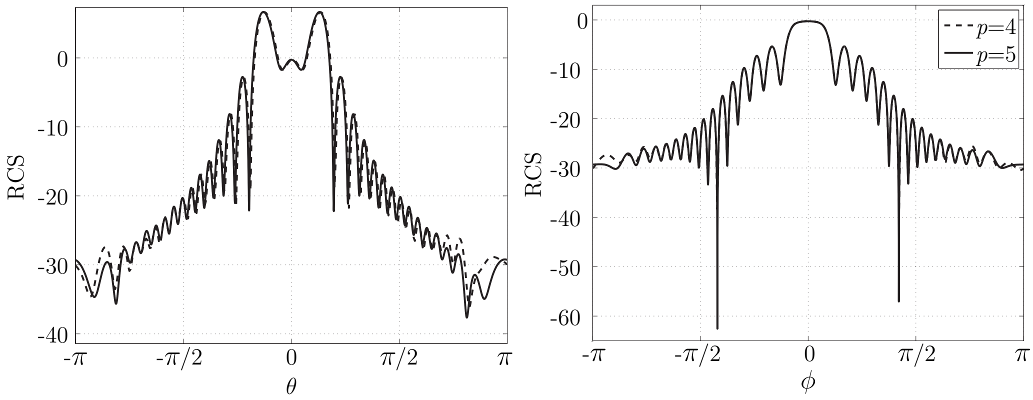

(a) Vertical polarization (b) Horizontal polarization

Figure 31: Scattering by a PEC NASA almond of characteristic length 8λ: bistatic RCS for a NEFEM solution with $p = 4$ and $p = 5$

components of the scattered field are represented over the almond surface in Figures 30 (b) and 30 (c), corresponding to a wave incident onto the tip of the almond.

Figure 31 shows bistatic RCS for vertical and horizontal polarizations. Two RCS patterns are displayed, for a NEFEM solution with $p = 4$ and $p = 5$ respectively. Results show a perfect agreement with published results [32], which are obtained with linear FEs in a tetrahedral mesh with 1 121 431 mesh nodes. Thus, this example shows the competitiveness of NEFEM compared to other formulations for more challenging applications. Even if a DG formulation is considered, i.e. duplicating nodes at inter-element faces, the computation requires less degrees of freedom to obtain similar accuracy, due to the good performance of NEFEM with coarse meshes and high-order approximations.

(a) Surface mesh (b) E_3 (c) H_3

Figure 32: Scattering by a PEC NASA almond of characteristic length 21λ: surface mesh on the almond and two components of the scattered field for a NEFEM solution with $p = 3$

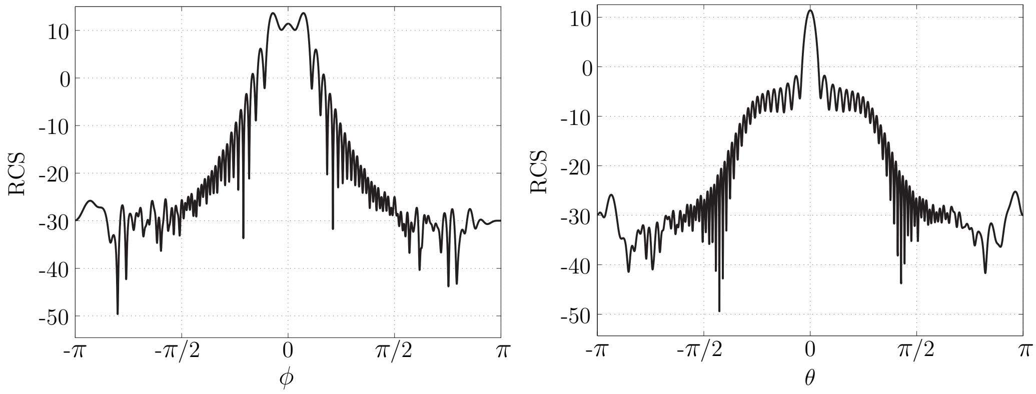

(a) Vertical polarization (b) Horizontal polarization

Figure 33: Scattering by a PEC NASA almond of characteristic length 21λ: bistatic RCS for a NEFEM solution with $p = 4$

Finally, the scattering by a PEC NASA almond of characteristic length 21λ is considered. The mesh has 48 699 elements with planar faces and 6 008 curved elements. Figure 32 shows the surface mesh on the almond and two components of the scattered field almond computed with NEFEM and $p = 3$, corresponding to a wave incident onto the tip of the almond. Bistatic RCS distribution for vertical and horizontal polarization are represented in Figure 33. Results compare well with published results [32], and again show the competitiveness of NEFEM for higher frequency problems. The tetrahedral mesh used in [32] has 51 342 008 linear elements, and approximately 8 million of nodes. With NEFEM and $p = 4$ the mesh has 2 million of nodes (including the duplication due to the DG formulation), requiring four times less degrees of freedom than using standard linear FEs.

R. Sevilla, S. Fernández-Méndez and A. Huerta
3D NURBS-Enhanced Finite Element Method
International Journal for Numerical Methods in Engineering, 88 (2); 103-125, 2011

4.2.3. PEC thin *plate*

Examples in previous sections show the advantages of NEFEM compared to several numerical techniques used by CEM community for the numerical solution of some classical tests and benchmark problems. However, possibilities of NEFEM still go beyond.

It is well known that, in the context of FEs, the size of the model is sometimes subsidiary of geometrical complexity and not only on solution itself. In particular, FE simulations of scattering by complex objects with small geometric details requires drastic h-refinement to capture geometry. Moreover, for scattering applications, small geometric details are influential in the solution, specially for high frequency problems, and a simplification of the geometry may lead to important discrepancies in computed RCS. Nevertheless, as it will be shown in this example, in the NEFEM context, when small is influential it does not imply small elements.

As noted earlier in Section 3, it is important to remark that the only restriction for a NEFEM element is that boundary edges and/or faces belong to one NURBS. It is neither necessary to locate nodes at boundary corners or edges (entities with $\mathcal{C}^0$ continuity) nor to refine the mesh near the boundary to capture geometry, it is exactly represented in NEFEM independently on the spatial discretization.

Scattering by a PEC *thin* plate of dimensions $\lambda \times 4\lambda/7 \times \lambda/22$ is considered. The small thickness of the plate with respect to wave length λ implies that h-refinement in standard FE meshes is controlled by the thickness of the plate, not by a desired number of nodes per wavelength.

Two standard FEM computational meshes are considered to compare accuracy of NEFEM computations. Figure 34 (a) shows a standard FE mesh with refinement towards the edges of the plate. Second mesh is a FEM mesh with a desired mesh size of about $\lambda/8$, see Figure 34 (b). As usual, a standard mesh generator needs to perform extra h-refinement to capture the small thickness of the plate, and minimum element size is, at least, $\lambda/22$. In contrast, element size for NEFEM is not controlled by small geometric features, and desired element size is maintained, even in the presence of singularities in the boundary. The plate is exactly represented by two NURBS surfaces with $\mathcal{C}^0$ continuity at the edges as illustrated in Figure 35 (a). A coarse *NEFEM mesh* is represented in Figure 35 (b). Note that, to obtain the desired element size, some elements contain an edge singularity inside one NURBS face, see a detailed view of a *NEFEM element* in Figure 36.

Preprint of
R. Sevilla, S. Fernández-Méndez and A. Huerta
3D NURBS-Enhanced Finite Element Method
International Journal for Numerical Methods in Engineering, 88 (2); 103-125, 2011

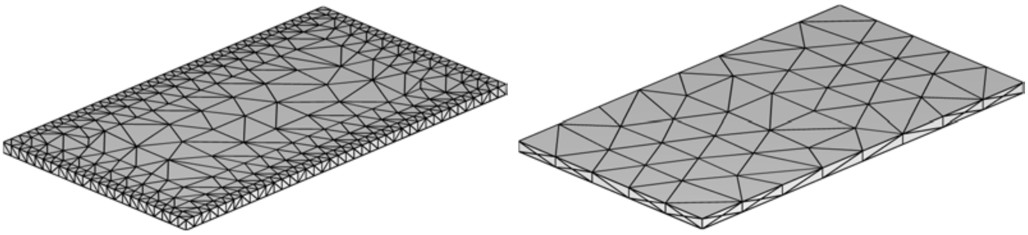

(a) Reference FEM mesh (b) FEM mesh

Figure 34: Scattering by a PEC thin plate: standard FE meshes

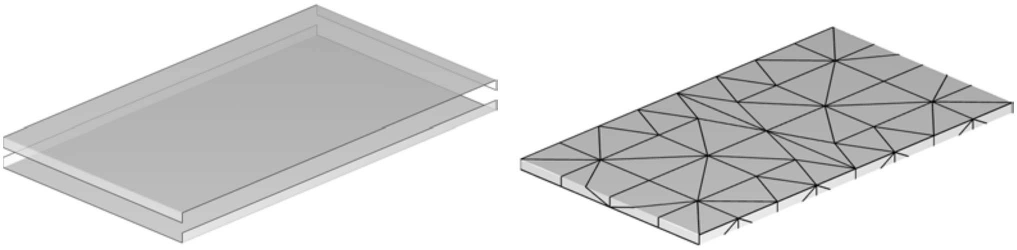

(a) NURBS surfaces (b) NEFEM mesh

Figure 35: Scattering by a PEC thin plate: NURBS surfaces (separated for visualization) and NEFEM coarse mesh with elements containing edge singularities

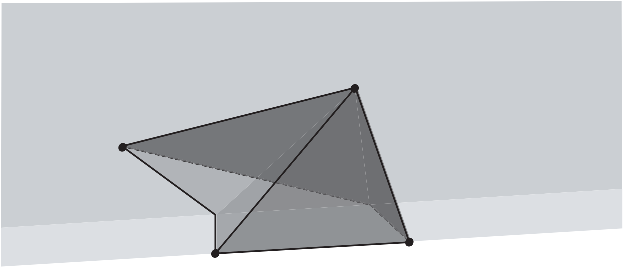

Figure 36: Detailed view of a NEFEM element containing an edge singularity in its boundary face

Preprint of
R. Sevilla, S. Fernández-Méndez and A. Huerta
3D NURBS-Enhanced Finite Element Method
International Journal for Numerical Methods in Engineering, 88 (2); 103-125, 2011

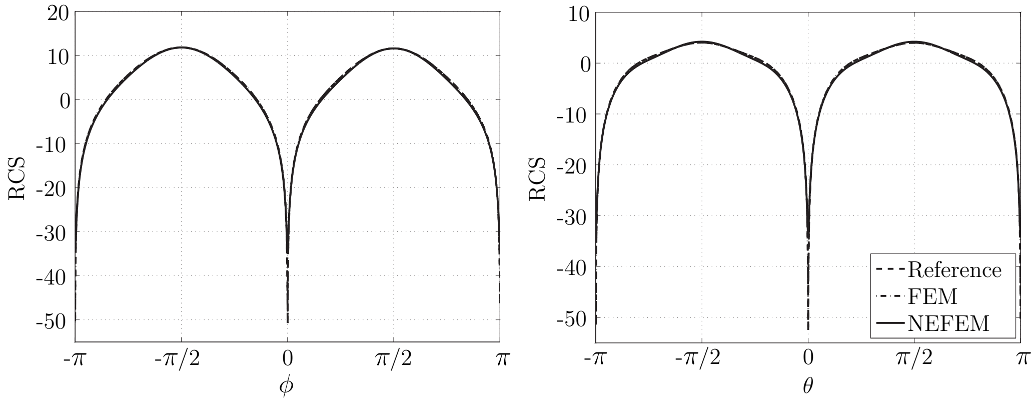

(a) Vertical polarization (b) Horizontal polarization

Figure 37: Scattering by a PEC thin plate: comparison of the RCS computed in the discretizations shown in Figures 34 (a), 34 (b) and 35 (a)

Figure 37 compares bistatic RCS distributions for vertical and horizontal polarizations. An excellent agreement is observed between three computations, showing the potential of coarse NEFEM meshes with elements containing geometric singularities. Maximum disagreement is obtained at singularities of the RCS due to its logarithmic scale, see [21]. In fact, error of the scattering width in $\mathcal{L}^2(-\pi,\pi)$ norm is 3.2×10^{-2} and 4.7×10^{-2} for vertical and horizontal polarizations respectively.

5. CONCLUDING REMARKS

This paper presents the extension of NEFEM to 3D domains. Exact CAD description of the geometrical model is considered, but only for the boundary of the computational domain. Thus, efficiency of classical FE techniques is preserved. The proposed methodology allows an efficient way to perform numerical integration over elements affected by NURBS boundaries. Moreover, trimmed and singular NURBS surfaces can be easily considered, making NEFEM a powerful methodology to work with industrial CAD models.

Numerical examples stress the drastic advantages of NEFEM compared to classical isoparametric and cartesian FEs, showing the importance of the geometrical model when coarse meshes and high-order of approximations are considered. The use of isoparametric or cartesian FEs leads to several orders of magnitude higher errors than using NEFEM. Some electromagnetic

Preprint of
R. Sevilla, S. Fernández-Méndez and A. Huerta
3D NURBS-Enhanced Finite Element Method
International Journal for Numerical Methods in Engineering, 88 (2); 103-125, 2011

scattering applications are considered to show the performance and benefits of the proposed method combined with a DG formulation. NEFEM is not only more accurate an efficient than isoparametric and cartesian FEs, but also is advantageous compared to other techniques used by CEM community. Finally, further possibilities and benefits of NEFEM are shown when very small geometric features compromises the use of standard methods that require excessive mesh refinement to capture geometry.

References

[1] F. Cirak, M. Ortiz, and P. Schröder, "Subdivision surfaces: a new paradigm for thin-shell finite-element analysis," *Internat. J. Numer. Methods Engng.*, vol. 47, no. 12, pp. 2039–2072, 2000.

[2] X.-J. Luo, M. S. Shephard, and J.-F. Remacle, "Influence of geometric approximation on the accuracy of higher order methods," Tech. Rep. 1, SCOREC, 2001.

[3] D. Xue and L. Demkowicz, "Control of geometry induced error in *hp* finite element (FE) simulations. I. Evaluation of FE error for curvilinear geometries," *Internat. J. Numer. Anal. Model.*, vol. 2, no. 3, pp. 283–300, 2005.

[4] O. C. Zienkiewicz and R. L. Taylor, *The Finite Element Method*, vol. 1. The basis. Butterwort-Heinemann, fifth ed., 2000.

[5] R. Sevilla, S. Fernández-Méndez, and A. Huerta, "Comparison of curved high-order finite elements," submitted.

[6] L. Piegl and W. Tiller, *The NURBS Book*. London: Springer-Verlag, 1995.

[7] F. Renken and G. Subbarayan, "NURBS-based solutions to inverse boundary problems in droplet shape prediction," *Comput. Methods Appl. Mech. Engrg.*, vol. 190, no. 11-12, pp. 1391–1406, 2000.

[8] D. Natekar, X. Zhang, and G. Subbarayan, "Constructive solid analysis: A hierarchical, geometry based meshless procedure for integrated design and analysis," *Comput. Aided Design*, vol. 36, pp. 473–486, 2004.

[9] K. Inoue, Y. Kikuchi, and T. Masuyama, "A NURBS finite element method for product shape design," *J. Engrg. Design*, vol. 16, no. 2, pp. 157–174, 2005.

[10] T. J. R. Hughes, J. A. Cottrell, and Y. Bazilevs, "Isogeometric analysis: CAD, finite elements, NURBS, exact geometry and mesh refinement," *Comput. Methods Appl. Mech. Engrg.*, vol. 194, no. 39–41, pp. 4135–4195, 2005.

[11] M. Rayasam, V. Srinivasan, and G. Subbarayan, "CAD inspired hierarchical partition of unity constructions for NURBS-based meshless design, analysis and optimization," *Internat. J. Numer. Methods Engrg.*, vol. 72, no. 12, pp. 1452–1489, 2007.

[12] R. Sevilla, S. Fernández-Méndez, and A. Huerta, "NURBS-enhanced finite element method (NEFEM)," *Internat. J. Numer. Methods Engrg.*, vol. 76, no. 1, pp. 56–83, 2008.

[13] R. Sevilla, S. Fernández-Méndez, and A. Huerta, "NURBS-enhanced finite element method (NEFEM) for Euler equations," *Internat. J. Numer. Methods Fluids*, vol. 57, no. 9, pp. 1051–1069, 2008.

[14] A. K. Dominek and H. T. Shamanski, "The almond test body," The Ohio State University ElectroScience Laboratory, Department of Electrical Engineering, Report 721929-9, NASA Langley Research Center, 1990.

[15] Q. Chen and I. Babuška, "The optimal symmetrical points for polynomial interpolation of real functions in the tetrahedron," *Comput. Methods Appl. Mech. Engrg.*, vol. 137, no. 1, pp. 89–94, 1996.

[16] J. S. Hesthaven, "Stable spectral methods on tetrahedral elements," *SIAM J. Numer. Anal.*, vol. 21, no. 6, pp. 2352–2380, 2000.

[17] T. Warburton, "An explicit construction of interpolation nodes on the simplex," *J. Eng. Math.*, vol. 56, no. 3, pp. 247–262, 2006.

[18] S. Wandzura and H. Xiao, "Symmetric quadrature rules on a triangle," *Comput. Math. Appl.*, vol. 45, no. 12, pp. 1829–1840, 2003.

[19] B. Szabó and I. Babuška, *Finite Element Analysis.* New York: John Wiley & Sons, 1991.

R. Sevilla, S. Fernández-Méndez and A. Huerta
3D NURBS-Enhanced Finite Element Method
International Journal for Numerical Methods in Engineering, 88 (2); 103-125, 2011

[20] R. F. Harrington, *Time-Harmonic Electromagnetic Fields.* New York: McGraw-Hill, 1961.

[21] C. A. Balanis, *Advanced Engineering Electromagnetics.* New York: John Wiley & Sons, 1989.

[22] U. Kangro and R. Nicolaides, "Spurious fields in time-domain computations of scattering problems," *IEEE Trans. Antennas Propagat.*, vol. 45, no. 2, pp. 228–234, 1997.

[23] R. J. LeVeque, *Numerical methods for conservation laws.* Lectures in Mathematics ETH Zürich, Basel: Birkhäuser Verlag, second ed., 1992.

[24] J. Donea and A. Huerta, *Finite Element Methods for Flow Problems.* Wiley, 2005.

[25] A. Taflove, *Computational Electrodynamics: The Finite-Difference Time-Domain Method.* Artech House, Inc., 1995.

[26] K. Morgan, O. Hassan, N. E. Pegg, and N. P. Weatherill, "The simulation of electromagnetic scattering in piecewise homogeneous media using unstructured grids," *Computat. Mech.*, vol. 25, pp. 438–447, 2000.

[27] P. D. Ledger, K. Morgan, O. Hassan, and N. P. Weatherill, "Plane wave $\mathbf{H}(\mathrm{curl};\Omega)$ conforming finite elements for Maxwell's equations," *Computat. Mech.*, vol. 31, no. 3-4, pp. 272–283, 2003.

[28] T. Huttunen, M. Malinen, and P. Monk, "Solving Maxwell's equations using the ultra weak variational formulation," *J. Comp. Phys*, vol. 223, no. 2, pp. 731–758, 2007.

[29] A. C. Woo, H. T. G. Wang, and M. J. Schub, "Benchmark radar targets for the validation of computational electromagnetics programs," *IEEE Trans. Antennas Propagat. Mag.*, vol. 35, no. 1, pp. 84–89, 1993.

[30] P. D. Ledger, K. Morgan, and O. Hassan, "Electromagnetic scattering simulation using an $\mathbf{H}(\mathrm{curl})$ conforming *hp* finite element method in three dimensions.," *Internat. J. Numer. Methods Fluids*, vol. 53, no. 8, pp. 1267–1296, 2007.

[31] M. J. Schuh, A. C. Woo, and M. P. Simon, "The monostatic/bistatic approximation," *IEEE Trans. Antennas Propagat. Mag.*, vol. 35, no. 4, pp. 76–78, 1994.

[32] M. E. Hachemi, O. Hassan, K. Morgan, D. Rowse, and N. Weatherill, "A low-order unstructured-mesh approach for computational electromagnetics in the time domain," *Philos. Trans. R. Soc. Lond. Ser. A Math. Phys. Eng. Sci.*, vol. 362, no. 1816, pp. 445–469, 2004.